nature neuroscience

Changes in synaptic structure underlie the developmental speeding of AMPA receptor–mediated EPSCs

Laurence Cathala[1,2], Noemi B Holderith[3], Zoltan Nusser[3], David A DiGregorio[2] & Stuart G Cull-Candy[1]

At many excitatory and inhibitory synapses throughout the nervous system, postsynaptic currents become faster as the synapse matures, primarily owing to changes in receptor subunit composition. The origin of the developmental acceleration of AMPA receptor (AMPAR)-mediated excitatory postsynaptic currents (EPSCs) remains elusive. We used patch-clamp recordings, electron microscopic immunogold localization of AMPARs, partial three-dimensional reconstruction of the neuropil and numerical simulations of glutamate diffusion and AMPAR activation to examine the factors underlying the developmental speeding of miniature EPSCs in mouse cerebellar granule cells. We found that the main developmental change that permits submillisecond transmission at mature synapses is an alteration in the glutamate concentration waveform as experienced by AMPARs. This can be accounted for by changes in the synaptic structure and surrounding neuropil, rather than by a change in AMPAR properties. Our findings raise the possibility that structural alterations could be a general mechanism underlying the change in the time course of AMPAR-mediated synaptic transmission.

The postsynaptic current at many synapses undergoes a marked change in time course during brain maturation. Early work demonstrated that at the endplate, this modification arises from a change in the subunit composition of postsynaptic acetylcholine receptors[1]. In the CNS, it is now well accepted that a similar switch in receptor subunit composition underlies the developmental change in glycinergic, GABAergic and NMDA receptor–mediated synaptic currents[2–4].

The time course of AMPAR-mediated EPSCs (AMPAR-EPSCs) also becomes faster during development[5–7], and this has been shown to be a critical determinant for information processing in the CNS[8]. Although changes in synaptic AMPAR subunit composition have been identified at some central synapses during development[9,10] and in certain forms of synaptic plasticity[11,12], the mechanism underlying the developmental speeding of AMPAR-EPSCs remains controversial. This is primarily due to the large number of factors that shape the AMPAR-EPSC time course. These factors include the time course of glutamate concentration change within the synaptic cleft (which is influenced by the structure of the synapse and the surrounding neuropil), the location and properties of glutamate transporters, the location of postsynaptic receptors with respect to the release site and the kinetic properties of AMPARs (for review, see ref. 13).

Here we examined the factors governing the developmental alterations of AMPAR-EPSCs in cerebellar granule cells, where an acceleration in kinetics has been identified[7,14]. This acceleration seems to have a critical impact on the integrative behavior of granule cells[14] and is governed predominantly by the speeding of the underlying miniature EPSCs (mEPSCs)[7,14]. Changes in the expression of AMPAR subunits during granule cell development[15,16], in particular increased expression of the GluR4-flop subunit that confers rapid kinetics[16], has raised the possibility that modifications in the molecular identity of AMPARs could underlie the EPSC speeding in granule cells. We found, however, that the acceleration of mEPSCs during granule cell maturation cannot be readily accounted for by functional changes in AMPAR properties. Instead, our results provide evidence that developmental changes in the neuropil (postsynaptic density (PSD) size, PSD location and diffusional space) can produce an alteration in the glutamate waveform that underlies the speeding of EPSCs.

RESULTS

To identify factors that determine the developmental change in the properties of AMPAR-mediated mEPSCs, we recorded from immature (postnatal days 7–8; 'P8') and adult (P35–78; 'P40') granule cells in acute slices. Granule cells remain electrically compact throughout development[14], allowing the examination of mEPSC kinetics with minimal space clamp error. We focused on mEPSCs to minimize the influence of any developmental changes in the synchrony of vesicular release[7] or release probability, both of which can affect the decay of evoked EPSCs[17,18].

[1]Department of Pharmacology, University College London, Gower Street, London WC1E 6BT, UK. [2]Physiologie Cérébrale, Centre National de la Recherche Scientifique UMR 8118, Université Paris 5, 45, rue des Saint-Pères, 75006 Paris, France. [3]Laboratory of Cellular Neurophysiology, Institute of Experimental Medicine, Hungarian Academy of Sciences, Szigony Street 43, 1083 Budapest, Hungary. Correspondence should be addressed to S.G.C.-C. (s.cull-candy@ucl.ac.uk).

Received 10 May; accepted 1 August; published online 18 September 2005; doi:10.1038/nn1534

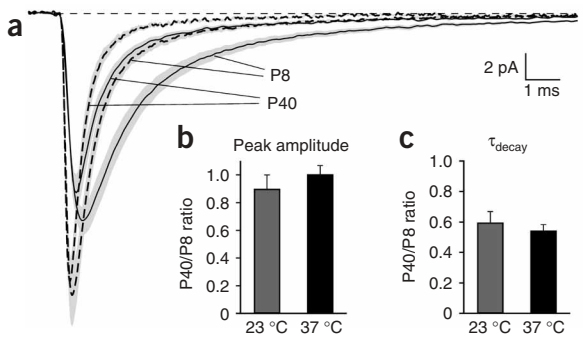

Figure 1 Developmental speeding of the AMPAR-mEPSC at 23 °C and 37 °C. (**a**) Superimposed mEPSC population averages at 23 °C at –70 mV (solid lines; gray shade indicates ±s.e.m.; $n = 19$ at P8 and $n = 20$ at P40) and 37 °C (dotted lines; $n = 20$ at P8 and $n = 20$ at P40). At 23 °C, the mean mEPSC peak amplitude was 15.8 ± 1.1 pA (coefficient of variation (c.v.) = 31 ± 7%; $n = 19$ cells) at P8 and 14.2 ± 1.1 pA (c.v. = 33 ± 8%; $n = 20$ cells) at P40 (both peak and c.v.; $P > 0.05$). The 10–90% rise time was 0.38 ± 0.02 ms at P8 and 0.23 ± 0.01 ms at P40 ($P < 0.01$). The weighted decay was 3.22 ± 0.29 ms at P8 and 1.92 ± 0.15 ms at P40 ($P < 0.01$). At 37 °C, the mean mEPSC peak amplitude was 22.1 ± 1.0 pA ($n = 39$) at P8 and 22.2 ± 0.9 pA ($n = 39$) at P40 ($P > 0.05$). The 10–90% rise-time was 0.18 ± 0.01 ms at P8 and 0.15 ± 0.004 ms at P40 ($P < 0.01$). The weighted decay was 1.33 ± 0.08 ms at P8 and 0.72 ± 0.03 ms at P40 ($P < 0.01$). (**b**) Bar graph showing the $peak_{P40}/peak_{P8}$ ratio at 23 °C and 37 °C. (**c**) Bar graph showing the τ_{wP40}/τ_{wP8} ratio at 23 °C and 37 °C.

Temperature dependence of mEPSC kinetics

To determine whether the developmental change in mEPSC kinetics is temperature dependent, we examined mEPSCs in P8 and P40 slices at 23 °C and 37 °C. There was no developmental change in peak amplitude or frequency at either temperature, but we observed a significant acceleration in the mEPSC rise and decay, as previously described[14] (**Fig. 1a**). The ratio of the mean mEPSC amplitudes of the two ages (P40 and P8; **Fig. 1b**) remained near 1 ($P > 0.05$) at both temperatures. The ratios of the weighted decay time constants (τ_{decay}) were also similar at the two temperatures ($P40\tau_w/P8\tau_w = 0.59 \pm 0.07$ at 23 °C, $n = 19$ and 0.54 ± 0.04 at 37 °C, $n = 39$; $P > 0.05$; **Fig. 1c**). The latter finding argues strongly that the developmental acceleration in mEPSC kinetics is independent of temperature. Since the uptake of glutamate by transporters is steeply temperature dependent, it seems unlikely that acceleration of the mEPSC time course arose from developmental enhancement of glutamate uptake. This conclusion is consistent with the absence of glia[18,19] within cerebellar glomeruli and with the lack of effect of transporter blockers within the first few milliseconds of single EPSCs at mossy fiber–granule cell synapses[7,18].

mEPSCs show linear *I-V* relationships at both P8 and P40

As AMPAR subunit expression changes during development[15,16], we next examined whether developmental acceleration in mEPSC kinetics could be directly ascribed to a modification of AMPAR properties. Because post-migratory granule cells do not express AMPARs on their cell bodies in slice preparations[20,21], receptor properties were deduced directly from mEPSC behavior.

AMPARs that lack GluR2 subunits show large single-channel conductances[22] and voltage-sensitive block by intracellular polyamines[11]. To test whether the synaptic contribution of GluR2-containing AMPARs changed during development, as described at certain other synapses[9,10], we examined mEPSCs over a range of membrane potentials. The current-voltage (*I-V*) relationships were linear at P8 and P40 ($n = 3$, both ages; **Fig. 2**), suggesting that synaptic AMPARs contain GluR2 subunits at both ages. These data also showed that the mEPSC decay was consistently slowed at depolarized potentials (**Fig. 2**). The P8 τ_{decay} increased by 80 ± 3% when cells were depolarized from −70 mV to +40 mV (data not shown; 23 °C; $n = 3$; $P < 0.05$), and the P40 τ_{decay} increased by 76.5 ± 17% when cells were depolarized from −80 mV to

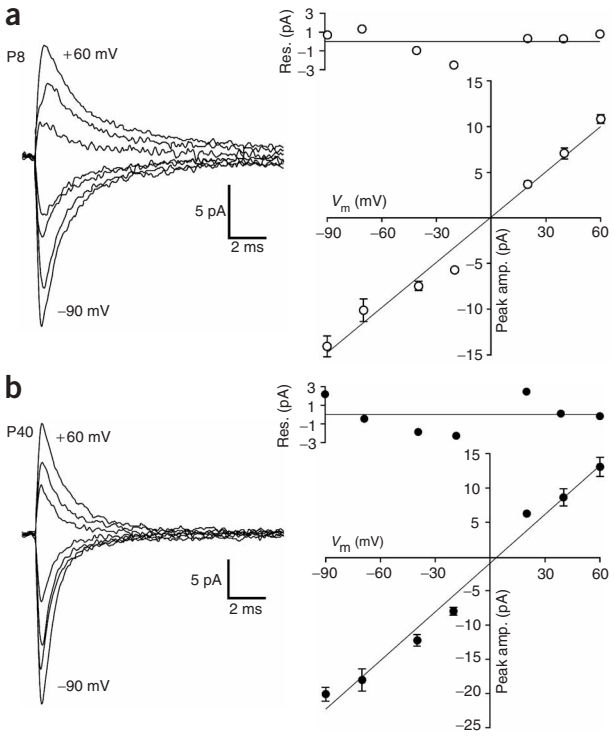

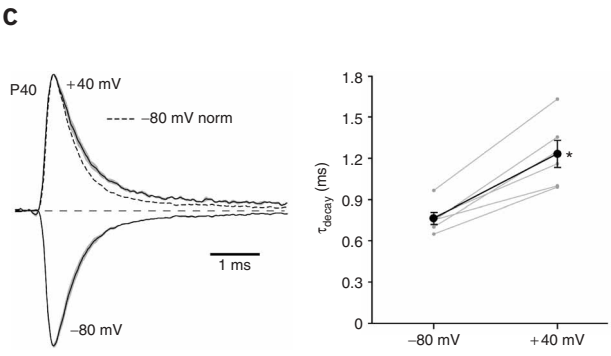

Figure 2 Voltage dependence of the AMPAR-mediated mEPSC. (**a**) Population average EPSC *I/V* relationship at P8 ($n = 3$) obtained between −90 and +60 mV at 23 °C. Lower right: *I/V* plot of pooled data (open circles) with a linear regression fit (straight line). Upper right: plot of residuals, indicating the error in the fit at each potential. (**b**) Population average EPSC *I/V* relationship at P40 ($n = 3$) at 23 °C. Lower right: *I/V* plot of pooled data. Upper right: plot of residuals. (**c**) Population average EPSCs (gray shade shows s.e.m.) at 37° C from P40 granule cells ($n = 6$, $V = -80$ mV and +40 mV). Mean responses were normalized. The response at the negative potential has been inverted (dotted line) and superimposed on the response at the positive potential. Summary plot at right shows voltage dependence of mEPSC τ_{decay}, with individual cells in gray, and mean (± s.e.m.) in black (*$P < 0.05$).

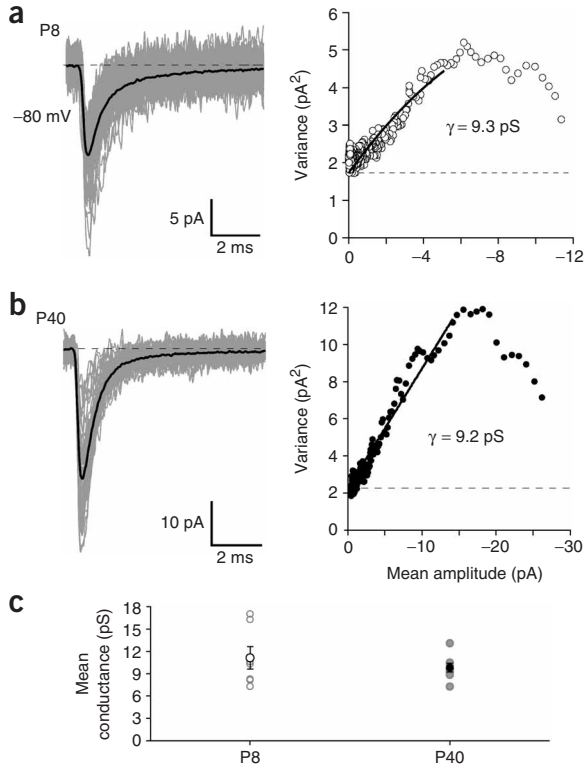

Figure 3 Mean single-channel conductance of AMPARs underlying mEPSCs remains constant between P8 and P40. (**a**) Left, 50 individual mEPSCs (gray traces) and average mEPSC (black trace) superimposed at P8. Right, a plot of their variance versus mean current ($n = 493$ mEPSCs). (**b**) Left, 50 individual mEPSCs (gray traces) and average mEPSC (black trace) superimposed at P40. Right, a plot of their variance versus mean current ($n = 178$ mEPSCs). The line indicates the fit of the initial two-thirds of the plot to the theoretical equation (see Methods). The dotted line indicates the baseline variance (1.73 pA^2 at P8 and 2.27 pA^2 at P40). The weighted mean conductance (γ) was 9.3 pS at P8 and 9.2 pS at P40. (**c**) Plot showing the mean single-channel conductance at both ages. Individual cells (open circles for P8, filled gray circles for P40) are shown along with the mean conductance at each age (± s.e.m.; black open circle for P8, black filled circle for P40). The estimated number of open channels at the peak was not significantly different (26 ± 3 at P8, and 34 ± 3 at P40; $P > 0.05$), as expected from the lack of difference in the mean peak amplitude[14]. All recordings were done at 37 °C.

+40 mV (**Fig. 2c**; 37 °C; $n = 6$; $P < 0.01$). As AMPAR kinetics become slower with depolarization[23], this result suggests that receptor gating properties contribute to EPSC decay kinetics at both ages.

Estimates of synaptic channel conductance at P8 and P40

The conductance of the AMPARs is critically dependent on subunit composition[22]. As the single-channel conductance of somatic AMPARs can change during granule cell migration[21], we examined whether the conductance of synaptic AMPARs differed between P8 and P40. We compared their weighted mean single-channel conductances (γ) using peak-scaled nonstationary fluctuation analysis at 37 °C (**Fig. 3**). We found no significant difference in γ between the two ages (P8: 11.2 ± 1.5 pS, $n = 7$ and P40: 9.8 ± 0.6 pS, $n = 8$; $P > 0.05$). These values are comparable to those obtained previously from P12 rats[17] and are in the same range as those obtained for recombinant heteromeric GluR2/GluR4 receptor assemblies[22], a subunit combination likely to be present in granule cells[16]. Because our γ estimates are similar to the largest estimates obtained from heteromeric GluR2-containing receptors (10 pS; ref. 22), the most likely explanation for our results is that, at both ages, the majority of the charge is carried by heteromeric GluR2-containing channels. This is consistent with the finding that AMPARs are predisposed to assemble as pairs of heteromeric dimers[24,25]. However, at neither age can we exclude a small contribution of GluR2 homomeric channels to mEPSCs, as small-conductance channels (<200 fS; ref. 22) have been observed in migrating granule cells[21].

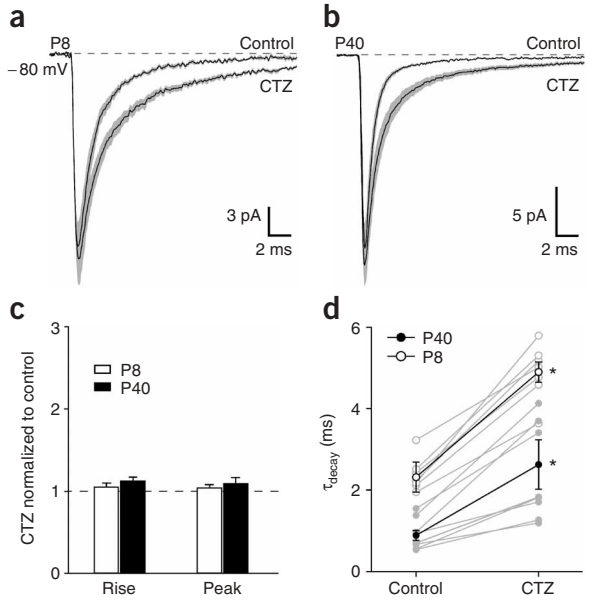

Cyclothiazide slows the mEPSC decay at both P8 and P40

AMPARs composed of the GluR2, -3 and -4 flop splice variants show faster desensitization rates than those containing flip variants[16,26]. In granule cells, GluR4-flop expression is initially lower than that of GluR4-flip and increases during development[16]. Therefore, we examined whether the acceleration of the mEPSC decay could be due to an enhanced contribution of the flop isoform to the synaptic AMPARs. To discriminate between flip and flop isoforms, we used a low concentration (10 μM) of cyclothiazide, an AMPAR modulator with preferential effects on flip variants[27]. At this concentration, unwanted presynaptic effects[28] of cyclothiazide were reduced, with no effect on mEPSC frequency (from 0.07 ± 0.03 Hz to 0.086 ± 0.04 Hz, $n = 7$ at P8; from 0.21 ± 0.08 to 0.24 ± 0.09, $n = 5$ at P40, both

Figure 4 Cyclothiazide (CTZ) slows the mEPSC decay equally at P8 and P40. (**a**) Population average EPSCs (solid line; gray shade shows ± s.e.m.) recorded from P8 granule cells under control conditions and in the presence of cyclothiazide (10 μM; $n = 7$, $V = -80$ mV). (**b**) Population average EPSCs recorded from P40 granule cells under control conditions and in the presence of cyclothiazide ($n = 9$). (**c**) Bar graph summarizing the effect of cyclothiazide on the 10–90% rise and peak amplitude at P8 and P40. (**d**) Plot showing the effect of cyclothiazide on the τ_{decay} of the EPSCs at P8 (open circles) and P40 (filled circles). Individual responses (gray filled and open circles) are shown along with mean response (± s.e.m., black filled and open circles; $^*P < 0.05$). The majority of data were obtained from recordings performed at 23 °C ($n = 7$ at P8 and $n = 5$ at P40). Recordings were also performed at 37 °C at P40 ($n = 4$). The relative slowing obtained at 23 °C and 37 °C was not significantly different, and thus data were pooled.

$P > 0.05$). We did not detect a significant change in the mean mEPSC peak amplitude (**Fig. 4**; $P > 0.05$) or in the rise time (**Fig. 4c**, $P > 0.05$), but cyclothiazide significantly increased the EPSC τ_{decay} (**Fig. 4a**,**b**,**d**, $P < 0.01$). The relative increase in τ_{decay} was comparable at both ages (210 ± 13% at P8 versus 260 ± 22% at P40, $P > 0.05$). These observations suggest that the increased expression in flop subunits[16] is unlikely to underlie the speeding in mEPSC time course.

Kynurenic acid preferentially accelerates P8 mEPSCs

We next considered whether the altered mEPSC time course could arise from a change in the spatiotemporal profile of glutamate experienced by the AMPARs (the effective glutamate waveform). The rapidly dissociating glutamate receptor antagonist kynurenic acid, which competes with glutamate during the rising phase of AMPAR-EPSCs, generates a block that is inversely related to transmitter concentration[29,30]. We used kynurenic acid to probe developmental alterations in the peak glutamate concentration[30] and in the glutamate waveform[18,29]. Application of kynurenic acid (0.5–1 mM) resulted in a reduction in the mEPSC peak amplitude that was similar at both ages (35 ± 4% at P8, $n = 7$ versus 29 ± 3% at P40, $n = 12$, $P > 0.05$; **Fig. 5a**,**b**, left), but accelerated the τ_{decay} only at P8 synapses (from 1.17 ± 0.14 ms to 0.75 ± 0.13 ms, $P < 0.01$; **Fig. 5a**,**b**, right). It is notable that in the presence of kynurenic acid, the P8 τ_{decay} approached the value observed at P40. These data suggest that the developmental speeding of mEPSCs may reflect a change in the effective glutamate waveform.

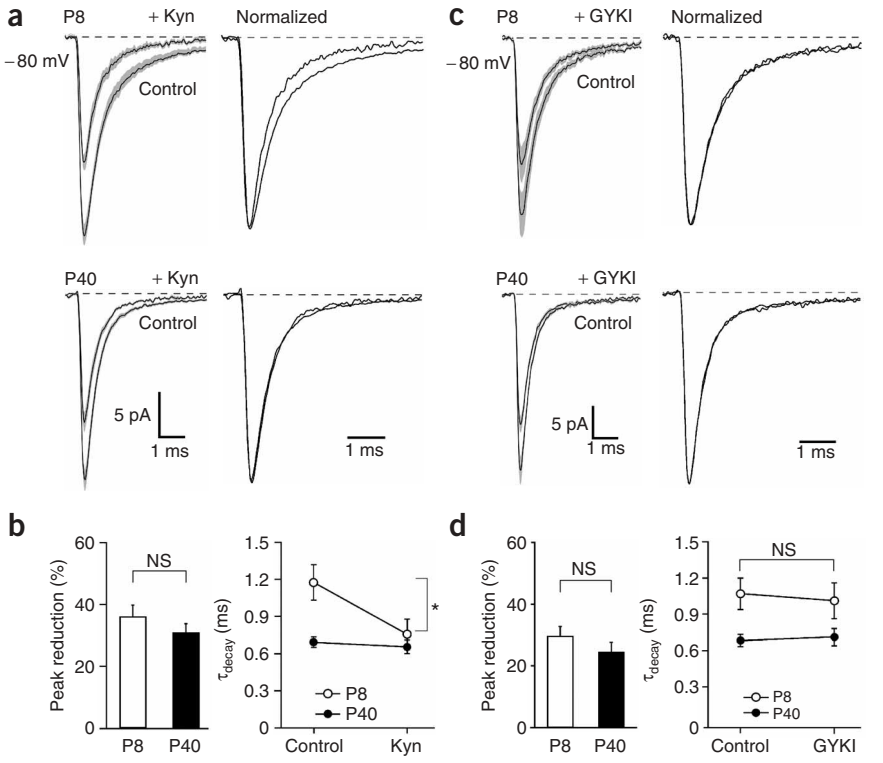

Figure 5 A low-affinity competitive antagonist preferentially accelerates P8 EPSCs. (**a**) Population average EPSCs (grey shading: ± s.e.m.) recorded from P8 and P40 granule cells in control and in kynurenic acid ('+Kyn'; $n = 7$ and $n = 12$, respectively; $V = -80$ mV). Superimposed normalized responses are shown at right. Similar concentrations were used for both ages (P8, 0.5–0.75 mM, mean = 0.7 ± 0.05 mM and P40, 0.5–1 mM, mean = 0.69 ± 0.05 mM; $P > 0.05$). (**b**) Left, bar graph showing percentage inhibition of mEPSC peak amplitude induced by kynurenic acid. Right, summary plot of kynurenic acid on mEPSC τ_{decay} (*$P < 0.05$; P40: 0.68 ± 0.03 ms versus 0.64 ± 0.05 ms in kynurenic acid, $P > 0.05$). (**c**) Population average EPSCs in control and in GYKI 53655 ('+GYKI'; $n = 5$ and $n = 7$, respectively, $V = -80$ mV). Superimposed normalized responses are shown at right. Similar concentration was used for both ages (P8, 1.5–2 μM, mean = 1.7 ± 0.12 mM and P40, 1-2 μM, mean = 1.4 ± 0.17 mM; $P > 0.05$). (**d**) Left, bar graph showing percentage reduction in EPSC peak amplitude induced by GYKI 53655 (29 ± 3%, $n = 5$ at P8 versus 24 ± 3%, $n = 7$ at P40, $P > 0.05$). Right, summary plot showing effect of GYKI 53655 on τ_{decay} (P8: 1.10 ± 0.13 ms versus 1.05 ± 0.14 ms in GYKI 53655 ($P > 0.05$); P40: 0.72 ± 0.05 ms versus 0.75 ± 0.07 ms ($P > 0.05$). All recordings at 37 °C.

To verify that the effect of kynurenic acid was due to a competitive interaction with glutamate, we examined the effect of a noncompetitive AMPAR antagonist (GYKI-53655) on mEPSCs. With concentrations of GYKI-53655 (1–2 μM) that produced a peak amplitude reduction similar to that produced by kynurenic acid ($P > 0.05$), we observed no change in τ_{decay} at either P8 or P40 (**Fig. 5c**,**d**, right). As GYKI-53655 preferentially blocks AMPARs over other ionotropic glutamate receptors, the lack of change in τ_{decay} rules out the presence of a slow kainate receptor–mediated component at both ages. Moreover, since both kynurenic acid and GYKI-53655 produced a similar fractional block at the two ages ($P > 0.05$), we conclude that the differential acceleration by kynurenic acid is unlikely to result from a developmental change in the AMPAR affinity for the antagonists or glutamate; instead, it is due to a change in the effective glutamate waveform.

Geometry of the glomerular neuropil and AMPAR distribution

The change in the effective glutamate waveform could result from either an alteration in the distribution of AMPARs in relation to the site of release, or a change in the spatiotemporal profile of glutamate in the synaptic cleft. To test directly the first possibility, we performed quantitative immunogold labeling of AMPARs at mossy fiber–granule cell synapses at both ages. To test the second, we used partial three-dimensional (3D) reconstructions and numerical simulations.

Postembedding electron microscopic immunogold localization of GluR1–GluR4 subunits showed that AMPARs were localized exclusively at asymmetrical synapses at both ages (**Fig. 6a**,**b**), as reported for a single age at other synapses[31,32]. However, the number of gold particles per single section of a synapse was significantly higher at P40 (2.3 ± 1.6, $n = 69$) than at P8 (1.3 ± 1.6, $n = 54$; $P < 0.01$). This was the consequence of a smaller proportion of immunonegative synapses (11 versus 39%), and of a more intense labeling at positive synapses. The shape of the distribution of gold particles along the synaptic specializations was not significantly different between the two ages ($P > 0.10$, Kolmogorov-Smirnov test; **Fig. 6d**), with a higher probability of labeling in the middle of a PSD (**Fig. 6c**). The vertical distribution of gold particles (particles' distance from the postsynaptic membrane) was indistinguishable between age groups (data not shown). The immunogold density was 202% higher at P40 than at P8 (4.3 ± 6.3 gold/μm at P8 versus 13.0 ± 9.4 gold/μm at P40; $P < 0.01$;

Fig. 6e). The increased number of gold particles per synaptic section reflected not only a higher AMPAR density, but also a smaller synaptic size at P40 (single cut length of synapse was 0.27 ± 0.11 μm at P8 versus 0.17 ± 0.4 μm at P40; $P < 0.01$; **Fig. 6f**; see also ref. 33).

To compare PSD area and shape more precisely between the two age groups, we made 3D reconstructions at both ages. P8 synapses were present in a greater number of sections and showed more convoluted shapes than P40 synapses (**Fig. 7a–e** versus **Fig. 7g–m**). Indeed, reconstructions showed that P8 synapses were larger and many demonstrated complex shapes (such as perforations; **Fig. 7f**), whereas P40 synapses were small and usually round in shape (**Fig. 7n**). The P8 PSD area was more than four times larger than that at P40 (0.10 ± 0.04 μm^2, $n = 14$ versus 0.024 ± 0.01 μm^2, $n = 13$; $P < 0.01$). These reconstructions also demonstrate that P8 mossy fiber terminals were much smaller and less convoluted than at P40, as described in rats[33]. At P8 the dendrite had a large proportion of its surface juxtaposed to the mossy fiber terminal in a cup-like fashion, and received several asymmetrical synapses (**Fig. 7f**). At P40, mossy fiber terminals established several asymmetrical synaptic junctions with several claw-like dendrites and dendritic fingers (**Fig. 7n**). In contrast with previous reconstructions[34], we found that the adult mossy fiber terminal can establish multiple junctions on the same dendritic finger. We also observed that the intersynapse distances appeared larger at P40, as described in rats[33]. There was no significant difference in the width of synaptic cleft between the two age groups (P8: 20.2 ± 1.7 nm, $n = 75$; P40: 19.6 ± 1.5 nm, $n = 28$; $P > 0.05$). The results of our 3D reconstructions together with quantitative AMPAR localizations suggest that structural changes could produce a difference in effective glutamate waveform.

Simulations of glutamate diffusion and AMPAR activation

As AMPARs were located exclusively at PSDs at both ages (**Fig. 6**), we examined the potential influence of the observed structural changes using numerical simulations of glutamate diffusion and AMPAR activation. We considered the effects of the following factors on mEPSC shape after the release of a single packet of glutamate: (i) decreased PSD size, (ii) change in granule cell dendritic shape (that is, increased number of diffusional sinks; **Fig. 7f** versus **Fig. 7n**), (iii) increased intersite distance and (iv) decreased number of neighboring synaptic junctions onto the same granule cell dendrite[33]. Because the contact surface between the mossy fiber terminal and a single granule cell dendrite is large in younger animals (**Fig. 7b**), we used simulations in which the glutamate released by one vesicle diffuses primarily in two dimensions (2D-geom; **Fig. 8a**, left). To simulate mature mEPSCs, we used a simplified 3D diffusional space[35] (3D-geom; **Fig. 8a**, right). For both ages, we used an AMPAR kinetic scheme[36] that predicted synaptic currents at rat mossy fiber–granule cell synapses[35]. We tested two PSD diameters (340 nm at P8 and 180 nm at P40) calculated from the 3D reconstructed PSD areas, as well as a third larger diameter of 500 nm (d500) to account for the large variability of PSD sizes at P8.

The peak amplitude of the simulated AMPAR open probability response ($P_{open}(t)$) decreased as PSD diameter increased for both geometries (**Fig. 8b**). This resulted from the fact that a significant proportion of the AMPARs were farther away from the source of glutamate and thus experienced a lower peak concentration[37]. The decrease in PSD diameter also led to an acceleration in rise time (up to 53% for 2D-geom and 46% for 3D-geom), with little effect on τ_{decay} of the $P_{open}(t)$ response (up to 16% for 2D-geom and 8% for 3D-geom; **Fig. 8b** insets). The geometry of the diffusional space had a greater effect on the τ_{decay} (decreased by up to 23% for d500) than on the rise time (decreased by up to 15% for d500; **Fig. 8c** for P8 PSD). Overall, the change in PSD size (P8 versus P40) combined with the change from 2D- to 3D-geom accelerated the rise time by 37% and τ_{decay} by 23% (**Fig. 8d**). The acceleration in rise time was comparable to the 25% acceleration obtained experimentally for mEPSCs at 37 °C (**Fig. 1a**). The speeding of τ_{decay}, however, was less than the 46% measured experimentally (**Fig. 1c**).

Currents mediated by glutamate spillover make a significant contribution to action potential–evoked EPSCs at mossy fiber–granule cell synapses in P25 rats[18]. Whether or not a spillover current contributes to mEPSCs is unknown, but it would depend on whether a single vesicle can release sufficient glutamate to diffuse onto neighboring PSDs of the

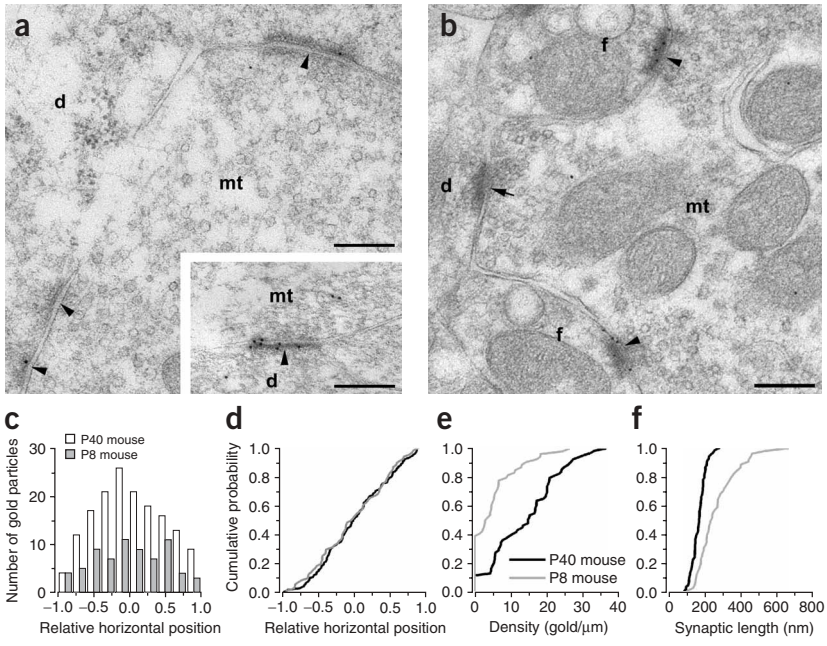

Figure 6 Electron micrographs showing the differences in AMPA receptor content of mossy fiber–granule cell synapses in P8 and P40 mice. (**a**,**b**) Postembedding immunogold labeling for the GluR1–GluR4 subunits in the granule cell layer at P8 (**a**) and P40 (**b**). (**a**) Asymmetrical synapses (arrowheads) made by a mossy fiber terminal (mt) with granule cell dendrites (d) are weakly labeled, having either zero or few particles. Inset shows one of a few synapses that showed somewhat stronger immunoreactivity. (**b**) Immunogold reaction in a P40 mouse demonstrates that two synapses (arrowheads) made by a mossy fiber terminal on fingers (f) of granule cell dendrites contain several gold particles. An unlabeled synapse (arrow) on a dendritic shaft (d) is also seen. (**c**) Horizontal normalized distribution of gold particles along the synaptic specialization. (**d**) Cumulative plot of the distribution of gold particles. Note that the distributions are very similar at both ages. (**e**) Cumulative probability plots showing the differences in the density of gold particles (given as number of gold particles per μm of synaptic cut length) between the two age groups. Note the larger numbers of immunonegative synapses at P8 compared to P40. (**f**) Synapses of young animals were larger and more variable in single cut length, whereas P40 synapses were smaller, as shown in the cumulative probability plots. Scale bars, 0.2 μm.

same granule cell. This is dependent not only on the intersite distance and the structure of the neuropil surrounding the synapses[38,39], but also on the likelihood that the neighboring PSDs are located on the same postsynaptic cell. At bouton-spine synapses, spillover of glutamate from single-release events is not sufficient to activate low-affinity AMPARs at neighboring spines (less than 1%)[38,39]. We examined AMPAR activation for both geometries, using the PSD intersite distance (640 nm) measured from 3D reconstructions in P18 rats[40]. In the 2D-geom simulations, the spillover-mediated response had a peak P_{open} of 0.02 (7.1% of peak P_{open} of direct response), whereas the peak P_{open} in the 3D-geom was smaller, 0.006 (less than 2% of the peak of direct response). Due to their slow rise time, the spillover current component slowed the decay of direct responses by 72% at P8 (**Fig. 8e**, left) and by 8% at P40 (**Fig. 8e**, right) when four neighbors were considered.

We also examined the influence of spillover-mediated responses at two additional intersite distances, 800 and 1,100 nm (**Fig. 8f**), which are likely in the range of that estimated from synaptic density for P8 and P40 glomeruli[33]. In the 2D-geom, all intersite distances produce a marked slowing of the direct response (7–72%), whereas in the 3D-geom the slowing of the decay was much less (0.5–14%). To approximate the overall influence of all observed structural changes, we compared the $P_{open}(t)$ for a P8 PSD with four neighbors 0.8 μm apart within the 2D-geom to that of a P40 PSD with two neighbors 1.1 μm apart within the 3D-geom. The τ_{decay} of a simulated 'P40'

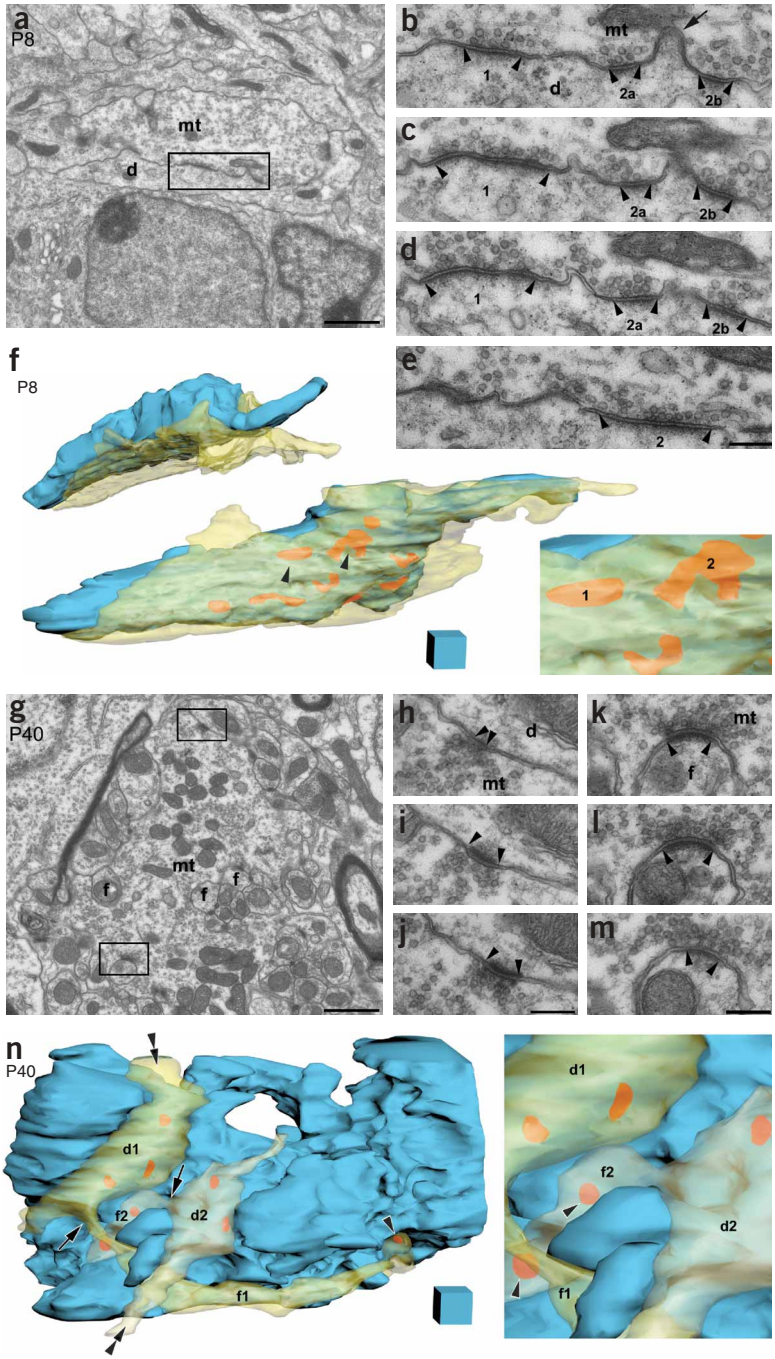

Figure 7 Analysis by electron microscopy of the cerebellar glomeruli in P8 and P40 mice. (**a**–**e**) A mossy fiber terminal (mt) establishes two synaptic junctions with a granule cell dendrite (d) in a P8 mouse. The dendrites do not invaginate into the mossy terminal. The boxed area is enlarged in panels **b**–**e**. Synapse 1 went through six serial sections (three are shown) and synapse 2 went through ten sections (four shown). A small piece of the nonsynaptic plasma membrane (arrow) protrudes into the terminal and splits the PSD of synapse 2 (into 2a and 2b). The edges of the specializations are marked by arrowheads. (**f**) Reconstruction in 3D of a mossy terminal and a granule cell dendrite in a P8 mouse. The mossy fiber terminal (blue) establishes several synaptic junctions on the granule cell dendrite (transparent yellow). The majority of the terminal from this view is visible only through the semi-transparent dendrite (green). Synaptic junctions (orange; nine of ten shown) show a large variability in size and shape (four out of ten synapses are perforated). Two arrowheads point to the synapses that are shown in **b**–**e**. The reconstructed terminal and the dendrite are viewed from a different angle in the inset. Right panel illustrates the synapses at a higher magnification (2.2×). (**g**–**m**) Micrographs demonstrate that a part of a large P40 mossy fiber terminal (mt) establishes synapses on several dendritic fingers (f; lower boxed area enlarged in **k**–**m**) and on dendritic shafts (d, upper boxed area, enlarged in **h**–**j**). (**n**) Synaptic junctions (orange) between a partially reconstructed P40 mossy fiber terminal (blue) and two granule cell dendrites. Dendrite 1 (d1, transparent dark yellow) approaches the terminal from the top (double arrowheads), gives rise to a long finger (f1, arrow marking the branch point) that courses below dendrite 2 and receives two synapses (arrowhead marks the visible one on the other side of the terminal). There are two more additional synaptic junctions directly on the shaft of d1. Dendrite 2 (light yellow) approaches from the bottom (double arrowheads), receives two junctions onto the shaft and gives rise to a short finger (f2, arrow marks the branch point) that receives two more synapses (marked with arrowheads in the inset). Inset, 2.2× magnification. They are smaller and are more homogeneous in size and shape compared to their P8 counterparts. Scale bars, 1 μm (**a**,**g**); 0.2 μm for all small panels; sides of the cubes in **f** and **n**, 0.5 μm.

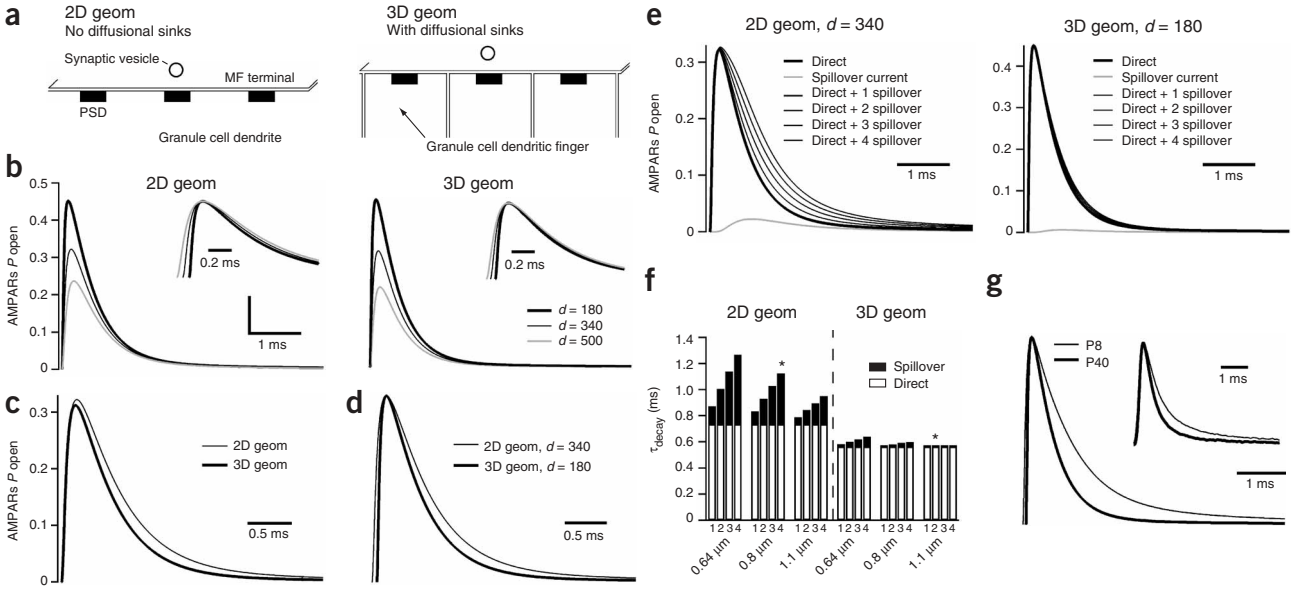

Figure 8 Influence of developmental changes in glomerular structure on simulated EPSCs. (**a**) Schematic representation of a cross-section of the immature (2D-geom; left) and mature glomerular geometries (3D-geom; right) used for simulation of glutamate diffusion. (**b**) Simulated receptor $P_{open}(t)$ from neurotransmitter released centered on different PSD diameters (d) in the 2D-geom (left) and in the 3D-geom (right). Inset, same traces normalized. In the 2D-geom for d500, P8 and P40: 10–90% rise was 0.111, 0.085 and 0.054 ms; τ_{decay} was 0.80, 0.74 and 0.67 ms). In the 3D-geom for d500, P8 and P40: 10–90% rise was 0.100 ms, 0.079 ms and 0.053 ms, and τ_{decay} was 0.613, 0.587 and 0.563 ms. (**c**) Superimposed $P_{open}(t)$ traces from **b** to show the effect of increased diffusional sinks ($d = 340$ nm). (**d**) Superposition of normalized simulated traces in which both the developmental decrease in PSD size and increased diffusional sinks are taken into account. (**e**) Simulated $P_{open}(t)$ traces in response to direct release (thick black) and spillover (gray trace) onto a site 640 nm away within the 2D-geom with PSD diameter of 340 nm (left panel) and 3D-geom with PSD diameter of 180 nm (right panel). Thin black traces are predictions of measured EPSCs if the spillover current was detected by the same postsynaptic cell with up to four neighboring PSDs. (**f**) Summary of the effect of intersite distance, number of neighbors and diffusional sinks on the decay of simulated $P_{open}(t)$. (**g**) Superposed normalized $P_{open}(t)$ approximating the observed developmental changes in glomerular structure (see * in **f**). The P8 $P_{open}(t)$ is a simulation from the 2D-geom with a 340-nm diameter PSD, an 800-nm intersite distance and four neighboring PSDs. The P40 $P_{open}(t)$ resulted from a simulation from a 3D-geom with a 180-nm diameter PSD, an 1,100-nm intersite distance and two neighboring PSDs. Inset, normalized population average mEPSC at 37 °C (from **Fig. 1a**).

mEPSC was now 49% faster than that of a 'P8' mEPSC (**Fig. 8g**), similar to the observed 46% acceleration of mEPSCs measured experimentally (**Fig. 1a**). We observed all the trends described above using three other kinetic schemes[29,41,42] (see ref. 35). For the same comparison as shown in **Fig. 8f**, the τ_{decay} of simulated 'P40' mEPSCs were respectively 49, 55 and 64% faster than that of 'P8' mEPSCs (data not shown). Thus we can account for the developmental speeding of mEPSCs by changes in synaptic structure without postulating a change in AMPAR properties.

DISCUSSION

Here we have shown that developmental changes in the glutamate waveform experienced by postsynaptic AMPARs can account for the observed acceleration in mEPSC decay. In contrast with many other types of excitatory and inhibitory synapses[1–4], we did not observe a change in receptor properties. Our data reveal that this alteration in effective glutamate waveform can be produced by a direct change in the cleft glutamate transient (due to increased diffusional sinks) and a change in receptor location (increased PSD size and intersite distance).

Changes in AMPAR properties do not explain EPSC speeding

We found no change in the voltage dependence or mean single-channel conductance of mEPSCs during development. This situation differs from that at others synapses where a developmental change has been detected both in AMPAR rectification[9,10] and single-channel conductance (L. Kelly, B.A. Clark, M. Farrant & S.G.C.-C. *Soc. Neurosci. Abstr.* 276.3, 2004). This suggests that, at both ages, a majority of synaptic AMPARs are likely to be heteromeric channel assemblies containing GluR2 subunits, possibly in conjunction with GluR4, which confers a large conductance to the channel[22] and is highly expressed throughout granule cell development[16]. The similarity in cyclothiazide sensitivity of the mEPSC decay indicates that the flip isoform contributes to synaptic AMPARs at both ages, consistent with the expression of the flip mRNA throughout granule cell development[15,16]. Moreover, these data also suggest that there was not a substantial increase in the contribution of the flop isoform to synaptic AMPARs. In young animals, we found that mEPSCs are observed only in a subset of granule cells. As the *in situ* hybridization experiments[15,16], samples both from less mature granule cells as well as those with functional synaptic connections, it is possible that an increase in flop subunit expression at the synapse is complete by the time of synapse formation[33]. Though our data indicate that flip isoforms continue to contribute to a majority of synaptic AMPARs, we do not exclude a small increase in the contribution of flop isoforms, since the flip isoform will tend to dominate both the desensitization properties[25] and cyclothiazide sensitivity[27] of AMPARs. Thus it seems unlikely that mEPSC acceleration in granule cells is mediated by a change in AMPAR properties that results from an increased contribution from flop isoforms. This conclusion is consistent with the finding that simulations of AMPARs containing predominantly flop isoforms[42] did not predict the EPSC time course at the mossy fiber–granule cell synapse[35,43].

Maintenance of peak mEPSC amplitude

Our immunogold localization experiments demonstrated a threefold increase in immunogold density and a fourfold decrease in PSD area during development. As a consequence, the total number of AMPARs appears to be reduced in adult animals. Our numerical simulations of AMPAR $P_{open}(t)$ predict that the observed developmental decrease in PSD size is expected to increase the mEPSC peak P_{open}. Hence the increased peak P_{open} appears to compensate for the decreased total receptor number per PSD. Our results indicate that alterations in the PSD area, the total number of AMPARs, and the peak P_{open} co-vary in a way that maintains a constant peak quantal amplitude throughout development.

Changes in glomerular structure underlie mEPSC speeding

Our numerical simulations reveal that a decrease in the PSD size may be the main determinant of the change in mEPSC rise time, whereas an increase in transmitter clearance and a decrease in the contribution of neighboring synaptic AMPARs may underlie the developmental acceleration in decay. Since AMPARs remain concentrated at PSDs during development, a redistribution of AMPARs from the extrasynaptic membrane to the PSD cannot account for the speeding of the effective glutamate waveform. To mimic the developmental change from a cup-like to a claw-like structure, we simulated an increased number of diffusional sinks. The resulting accelerated clearance of glutamate produced a substantial speeding of the mEPSC decay.

Our simulations also suggest that a single packet of glutamate can produce a spillover current that contributes to the mEPSC decay, but only under certain conditions. The developmental increase in diffusional sinks, the increased intersite distance, and the reduced likelihood that the neighboring PSDs are on the same granule cell would favor a prominent spillover contribution to the mEPSC decay at the mossy fiber–granule cell synapse in young mice, but not in the adult. The slow mEPSC decay in rat granule cells (P10–P14) has previously been suggested to reflect a delayed clearance of glutamate from the synaptic cleft[17]. However, our simulations mimicking P8 EPSCs suggest that spillover onto neighboring sites is also likely to contribute to the slow decay at P10–P14, an age at which the intersite distances appear to be shorter than at P8 (ref. 33).

Since it has been suggested that the time course of neurotransmitter release from individual vesicles may also change during development[44], it is possible that a slow tail of glutamate flux could contribute to the slow P8 mEPSC kinetics. Although we cannot rule out this possibility for young animals, as was possible for action potential–evoked spillover current at the mossy fiber–granule cell synapse at P25 (ref. 35), our simulations indicate that the change in effective glutamate waveform can be accounted for by the observed structural changes.

Impact of mEPSC speeding caused by structural changes

mEPSCs are important not only for shaping the time course of action potential–evoked synaptic transmission, but they can also have a role in homeostatic and activity-dependent neuronal processes[45,46]. Thus, alterations in mEPSC time course may have a broad impact on neuronal function. At the mossy fiber–granule cell synapse, a developmental decrease in the contribution of quantal spillover currents to mEPSCs will improve precision of EPSP-spike coupling[14], whereas the slow action potential–evoked spillover currents would serve to improve reliability[18]. In the adult, this may promote synchronization of postsynaptic granule cell firing while maintaining precise EPSP-spike coupling. The slow AMPAR-mEPSCs in granule cells from young animals could potentially serve to increase the depolarization associated with each quanta, such that the Mg^{2+} block of synaptic NMDARs[14] is more effectively relieved in order to mediate plasticity and other Ca^{2+}-dependent processes[45]. Moreover, the shorter intersite distances at immature synapse would be expected to result in larger spillover currents that could increase their contribution to short-term depression[40].

Speeding of mEPSCs may also occur at other synapses in which there is a significant decrease in PSD size, a change in receptor localization or an increase in diffusional sinks. This is particularly applicable to synapses where there are multiple closely spaced synaptic contacts between the pre- and postsynaptic neuron[47]. For example, in the calyx of Held, where changes in AMPAR subunits do not account for the developmental EPSC speeding[48], developmental changes in structure[49] similar to those of the mossy fiber–granule cell synapse could account for the observed speeding. A large body of evidence now suggests that changes in spine structure (for example, PSD size, geometry, spine splitting and transformation to multisynaptic junctions) and density are associated with development and synaptic plasticity (for review, see ref. 50). It remains to be seen whether structural changes found throughout the brain during development and during normal synaptic function could potentially serve as a mechanism for controlling the time course of synaptic transmission.

METHODS

Electrophysiology. Whole-cell recordings were performed from parasagittal cerebellar slices (200–250 μm) from C57BL/6J mice at ages P7–P78, as described previously[14]. mEPSCs were recorded at about 23 °C or 37 °C with a solution containing 125 mM NaCl, 2.5 mM KCl, 2 mM $CaCl_2$, 1 mM $MgCl_2$, 26 mM $NaHCO_3$, 1.25 mM NaH_2PO_4 and 25 mM glucose, bubbled with 95% O_2/5% CO_2 (pH 7.4) with blockers of NMDA receptors (20 μM 7-chlorokynurenate and 20 μM D-AP5) and GABAergic and glycinergic receptors (100 μM picrotoxin or 10 μM SR95537 and 1 μM strychnine). The pipette solution contained 130 mM potassium gluconate, 10 mM HEPES, 5 mM EGTA, 4 mM NaCl, 1 mM $CaCl_2$, 2 mM Mg-ATP (adjusted to pH 7.3 with KOH). For the *I/V* relationships, potassium gluconate was replaced by 130 mM CsCl, and TEA (5 mM), QX314 (1 mM) and spermine (0.1 mM) were added[11].

Postembedding immunogold localization of AMPARs. Postembedding reactions were carried out as previously described[18], on 80-nm thick sections of Lowicryl resin-embedded cerebella from four mice in each age group. For immunolabeling, we used rabbit antibodies to GluR1–GluR4 at a final concentration of 4–11 μg/ml (ref. 31). The immunoreactions were carried out in parallel for both age groups, to minimize procedural variation. Gold particles were counted from randomly selected synapses with clearly visible synaptic clefts. We measured PSD lengths, the lateral distance of each gold particle from the edge of the PSD and the vertical distance of each gold particle from the postsynaptic membrane. A gold particle was considered to be associated with the plasma membrane if the middle of the particle was within 80 nm (±2 s.d. of the Gaussian fitted to the vertical particle distribution) from the middle of the lipid bilayer. Nonspecific immunogold density was calculated over mitochondria. Immunoparticle densities (in particles/μm^2) were calculated in particle per effective membrane area (effective membrane area = membrane length × 80 nm) over the synaptic specializations. Linear immunoparticle densities (in particles/μm) were calculated after the subtraction of nonspecific labeling density.

3D reconstructions of the mossy fiber–granule cell glomerulus. Pieces of cerebellum tissue prepared for morphological examinations were re-embedded from the dorsal part of folium 3 in both age groups (to ensure the comparison of synapses of the same area), and long serial electron microscope sections (80–100 sections) were cut for 3D reconstructions. Digital images of glomeruli were taken at each serial section. Synapses were included in our measurements if the synaptic cleft was clearly visible. The PSD length and the synaptic cleft width were measured in each section. The PSD area was calculated by multiplying each length with the section thickness. Reconstruct software (J.C. Fiala, Biology Department, Boston University, http://synapses.bu.edu/) was used for 3D reconstruction.

A detailed description of the mEPSC analysis, tissue preparation for electron microscopy and immunocytochemistry, and numerical simulations of glutamate diffusion and AMPAR responses are available in **Supplementary Methods** online.

Note: Supplementary information is available on the Nature Neuroscience website.

ACKNOWLEDGMENTS

This work was supported by a Wellcome Trust Programme Grant (S.G.C.-C.), a Wellcome Trust Travelling Fellowship (L.C.) and the Centre National de la Recherche Scientifique (L.C. and D.A.D.). S.G.C.-C. holds a Royal Society-Wolfson Award. Z.N. acknowledges receipt of a Wellcome Trust International Senior Research Fellowship, an International Scholarship from Howard Hughes Medical Institute and a Postdoctoral Fellowship from the Boehringer Ingelheim Fund. We thank E. Molnár for providing the anti-pan-AMPA antibody and M. Köllö for his help with the 3D reconstruction. We thank T. Nielsen and J. Rothman for provision of software, S. Brickley, M. Farrant, V. Nägerl and A. Silver for helpful discussions, and B. Barbour, P. DiGregorio, M. Farrant, A. Marty, T. Nielsen, A. Silver and A. Roth for comments on the manuscript.

COMPETING INTERESTS STATEMENT

The authors declare that they have no competing financial interests.

Published online at http://www.nature.com/natureneuroscience/
Reprints and permissions information is available online at http://npg.nature.com/reprintsandpermissions/

1. Mishina, M. *et al.* Molecular distinction between fetal and adult forms of muscle acetylcholine receptor. *Nature* **321**, 406–411 (1986).
2. Takahashi, T., Momiyama, A., Hirai, K., Hishinuma, F. & Akagi, H. Functional correlation of fetal and adult forms of glycine receptors with developmental changes in inhibitory synaptic receptor channels. *Neuron* **9**, 1155–1161 (1992).
3. Tia, S., Wang, J.F., Kotchabhakdi, N. & Vicini, S. Developmental changes of inhibitory synaptic currents in cerebellar granule neurons: role of $GABA_A$ receptor alpha 6 subunit. *J. Neurosci.* **16**, 3630–3640 (1996).
4. Hestrin, S. Developmental regulation of NMDA receptor-mediated synaptic currents at a central synapse. *Nature* **357**, 686–689 (1992).
5. Bellingham, M.C., Lim, R. & Walmsley, B. Developmental changes in EPSC quantal size and quantal content at a central glutamatergic synapse in rat. *J. Physiol. (Lond.)* **511**, 861–869 (1998).
6. Taschenberger, H. & von Gersdorff, H. Fine-tuning an auditory synapse for speed and fidelity: developmental changes in presynaptic waveform, EPSC kinetics, and synaptic plasticity. *J. Neurosci.* **20**, 9162–9173 (2000).
7. Wall, M.J., Robert, A., Howe, J.R. & Usowicz, M.M. The speeding of EPSC kinetics during maturation of a central synapse. *Eur. J. Neurosci.* **15**, 785–797 (2002).
8. London, M., Schreibman, A., Hausser, M., Larkum, M.E. & Segev, I. The information efficacy of a synapse. *Nat. Neurosci.* **5**, 332–340 (2002).
9. Lawrence, J.J. & Trussell, L.O. Long-term specification of AMPA receptor properties after synapse formation. *J. Neurosci.* **20**, 4864–4870 (2000).
10. Kumar, S.S., Bacci, A., Kharazia, V. & Huguenard, J.R. A developmental switch of AMPA receptor subunits in neocortical pyramidal neurons. *J. Neurosci.* **22**, 3005–3015 (2002).
11. Liu, S.Q. & Cull-Candy, S.G. Synaptic activity at calcium-permeable AMPA receptors induces a switch in receptor subtype. *Nature* **405**, 454–458 (2000).
12. Benke, T.A., Luthi, A., Isaac, J.T. & Collingridge, G.L. Modulation of AMPA receptor unitary conductance by synaptic activity. *Nature* **393**, 793–797 (1998).
13. Jonas, P. The time course of signaling at central glutamatergic synapses. *News Physiol. Sci.* **15**, 83–89 (2000).
14. Cathala, L., Brickley, S., Cull-Candy, S. & Farrant, M. Maturation of EPSCs and intrinsic membrane properties enhances precision at a cerebellar synapse. *J. Neurosci.* **23**, 6074–6085 (2003).
15. Monyer, H., Seeburg, P.H. & Wisden, W. Glutamate-operated channels: developmentally early and mature forms arise by alternative splicing. *Neuron* **6**, 799–810 (1991).
16. Mosbacher, J. *et al.* A molecular determinant for submillisecond desensitization in glutamate receptors. *Science* **266**, 1059–1062 (1994).
17. Silver, R.A., Cull-Candy, S.G. & Takahashi, T. Non-NMDA glutamate receptor occupancy and open probability at a rat cerebellar synapse with single and multiple release sites. *J. Physiol. (Lond.)* **494**, 231–250 (1996).
18. DiGregorio, D.A., Nusser, Z. & Silver, R.A. Spillover of glutamate onto synaptic AMPA receptors enhances fast transmission at a cerebellar synapse. *Neuron* **35**, 521–533 (2002).
19. Xu-Friedman, M.A., Harris, K.M. & Regehr, W.G. Three-dimensional comparison of ultrastructural characteristics at depressing and facilitating synapses onto cerebellar Purkinje cells. *J. Neurosci.* **21**, 6666–6672 (2001).
20. Silver, R.A., Colquhoun, D., Cull-Candy, S.G. & Edmonds, B. Deactivation and desensitization of non-NMDA receptors in patches and the time course of EPSCs in rat cerebellar granule cells. *J. Physiol. (Lond.)* **493**, 167–173 (1996).
21. Smith, T.C., Wang, L.Y. & Howe, J.R. Heterogeneous conductance levels of native AMPA receptors. *J. Neurosci.* **20**, 2073–2085 (2000).
22. Swanson, G.T., Kamboj, S.K. & Cull-Candy, S.G. Single-channel properties of recombinant AMPA receptors depend on RNA editing, splice variation, and subunit composition. *J. Neurosci.* **17**, 58–69 (1997).
23. Otis, T.S., Wu, Y.C. & Trussell, L.O. Delayed clearance of transmitter and the role of glutamate transporters at synapses with multiple release sites. *J. Neurosci.* **16**, 1634–1644 (1996).
24. Mansour, M., Nagarajan, N., Nehring, R.B., Clements, J.D. & Rosenmund, C. Heteromeric AMPA receptors assemble with a preferred subunit stoichiometry and spatial arrangement. *Neuron* **32**, 841–853 (2001).
25. Brorson, J.R., Li, D. & Suzuki, T. Selective expression of heteromeric AMPA receptors driven by flip-flop differences. *J. Neurosci.* **24**, 3461–3470 (2004).
26. Koike, M., Tsukada, S., Tsuzuki, K., Kijima, H. & Ozawa, S. Regulation of kinetic properties of GluR2 AMPA receptor channels by alternative splicing. *J. Neurosci.* **20**, 2166–2174 (2000).
27. Partin, K.M., Patneau, D.K. & Mayer, M.L. Cyclothiazide differentially modulates desensitization of alpha-amino-3-hydroxy-5-methyl-4-isoxazolepropionic acid receptor splice variants. *Mol. Pharmacol.* **46**, 129–138 (1994).
28. Diamond, J.S. & Jahr, C.E. Asynchronous release of synaptic vesicles determines the time course of the AMPA receptor-mediated EPSC. *Neuron* **15**, 1097–1107 (1995).
29. Diamond, J.S. & Jahr, C.E. Transporters buffer synaptically released glutamate on a submillisecond time scale. *J. Neurosci.* **17**, 4672–4687 (1997).
30. Yamashita, T., Ishikawa, T. & Takahashi, T. Developmental increase in vesicular glutamate content does not cause saturation of AMPA receptors at the calyx of held synapse. *J. Neurosci.* **23**, 3633–3638 (2003).
31. Nusser, Z. *et al.* Cell type and pathway dependence of synaptic AMPA receptor number and variability in the hippocampus. *Neuron* **21**, 545–559 (1998).
32. Tanaka, J. *et al.* Number and density of AMPA receptors in single synapses in immature cerebellum. *J. Neurosci.* **25**, 799–807 (2005).
33. Hamori, J. & Somogyi, J. Differentiation of cerebellar mossy fiber synapses in the rat: a quantitative electron microscope study. *J. Comp. Neurol.* **220**, 365–377 (1983).
34. Jakab, R.L. & Hamori, J. Quantitative morphology and synaptology of cerebellar glomeruli in the rat. *Anat. Embryol. (Berl.)* **179**, 81–88 (1988).
35. Nielsen, T.A., DiGregorio, D.A. & Silver, R.A. Modulation of glutamate mobility reveals the mechanism underlying slow-rising AMPAR EPSCs and the diffusion coefficient in the synaptic cleft. *Neuron* **42**, 757–771 (2004).
36. Hausser, M. & Roth, A. Dendritic and somatic glutamate receptor channels in rat cerebellar Purkinje cells. *J. Physiol. (Lond.)* **501**, 77–95 (1997).
37. Franks, K.M., Bartol, T.M., Jr. & Sejnowski, T.J. A Monte Carlo model reveals independent signaling at central glutamatergic synapses. *Biophys. J.* **83**, 2333–2348 (2002).
38. Rusakov, D.A. The role of perisynaptic glial sheaths in glutamate spillover and extracellular Ca^{2+} depletion. *Biophys. J.* **81**, 1947–1959 (2001).
39. Barbour, B. An evaluation of synapse independence. *J. Neurosci.* **21**, 7969–7984 (2001).
40. Xu-Friedman, M.A. & Regehr, W.G. Ultrastructural contributions to desensitization at cerebellar mossy fiber to granule cell synapses. *J. Neurosci.* **23**, 2182–2192 (2003).
41. Partin, K.M., Fleck, M.W. & Mayer, M.L. AMPA receptor flip/flop mutants affecting deactivation, desensitization, and modulation by cyclothiazide, aniracetam, and thiocyanate. *J. Neurosci.* **16**, 6634–6647 (1996).
42. Raman, I.M. & Trussell, L.O. The mechanism of alpha-amino-3-hydroxy-5-methyl-4-isoxazolepropionate receptor desensitization after removal of glutamate. *Biophys. J.* **68**, 137–146 (1995).
43. Saftenku, E.E. Modeling of slow glutamate diffusion and AMPA receptor activation in the cerebellar glomerulus. *J. Theor. Biol.* **234**, 363–382 (2005).
44. Renger, J.J., Egles, C. & Liu, G. A developmental switch in neurotransmitter flux enhances synaptic efficacy by affecting AMPA receptor activation. *Neuron* **29**, 469–484 (2001).
45. Murphy, T.H. *et al.* Differential regulation of calcium/calmodulin-dependent protein kinase II and p42 MAP kinase activity by synaptic transmission. *J. Neurosci.* **14**, 1320–1331 (1994).
46. McKinney, R.A., Capogna, M., Durr, R., Gahwiler, B.H. & Thompson, S.M. Miniature synaptic events maintain dendritic spines via AMPA receptor activation. *Nat. Neurosci.* **2**, 44–49 (1999).
47. Walmsley, B., Alvarez, F.J. & Fyffe, R.E. Diversity of structure and function at mammalian central synapses. *Trends Neurosci.* **21**, 81–88 (1998).
48. Koike-Tani, M., Saitoh, N. & Takahashi, T. Mechanisms underlying developmental speeding in AMPA-EPSC decay time at the calyx of Held. *J. Neurosci.* **25**, 199–207 (2005).
49. Taschenberger, H., Leao, R.M., Rowland, K.C., Spirou, G.A. & von Gersdorff, H. Optimizing synaptic architecture and efficiency for high-frequency transmission. *Neuron* **36**, 1127–1143 (2002).
50. Segal, M. Dendritic spines and long-term plasticity. *Nat. Rev. Neurosci.* **6**, 277–284 (2005).